Research paper

Effect of conjugation degree and delocalized π-system on the photocatalytic activity of single layer g-C_3N_4

Anye Shi [a],[1], Huihui Li [a],[*],[1], Shu Yin [b], Bin Liu [a], Jiachi Zhang [a],[*], Yuhua Wang [a]

[a] National & Local Joint Engineering Laboratory for Optical Conversion Materials and Technology, Lanzhou University, 222 South Tianshui Road, Lanzhou 730000, PR China
[b] Institute of Multidisciplinary Research for Advanced Materials, Tohoku University, 2-1-1 Katahira, Aoba-ku, Sendai 980-8577, Japan

ARTICLE INFO

ABSTRACT

Single layer g-C_3N_4 could be obtained from a protonic acid treatment of g-C_3N_4 or a new sandwich-like orientation growth of melamine. Through the self-assembly of melamine and polyacrylamide by hydrogen bonds and electrostatic interactions, g-C_3N_4, with extended planarized atomic single layer, exhibits superiority in both photocatalytic hydrogen evolution and photocatalytic degradation under visible light irradiation. Besides low efficiency, the acid exfoliation will destroy the delocalized π-system by inducing O atoms. The decrease of conjugation degree increases the optical gaps, making it hard for g-C_3N_4 to capture photons. On the contrary, the facile sandwich-like orientation growth of melamine highly keeps the conjugation degree of g-C_3N_4 and extends its delocalized π-system. Such single layer g-C_3N_4 is more active even better than N-doped TiO_2 under visible light irradiation.

© 2017 Elsevier B.V. All rights reserved.

1. Introduction

In order to benefit from its typical advantage of increasing generated free charge carriers in two-dimensional conformation, as a cost effective metal-free photocatalyst, planarized g-C_3N_4 with ultra-thin thickness on the nanometer has been considered a potential excellent photocatalyst for both hydrogen evolution and organic pollutants degradation [1–11]. The existing methods to obtain ultrathin g-C_3N_4 by exfoliation of pristine g-C_3N_4 can be divided into liquid ultrasonic exfoliation [1–4], chemical exfoliation [5,6], thermal oxidation etching [7], and bottom-up polycodension [8–11]. However, besides environmental pollution, these methods have bred many other problems, such as low yield, complex steps, and time-consuming. One of the most serious problems is that g-C_3N_4 nanosheets are thicker than 2 nm and composed of several layers but not of a single atomic layer [5]. Among various above strategies, acid exfoliation is actually the one in which atomic single layer g-C_3N_4 could be obtained. However, to destroy the interlayer Van der Waals force, severe reaction conditions, such as drastic acid treatment and repeated heating process, can not prevent the planar structure destruction [5–7]. Thus, it is necessary to develop a real single layer g-C_3N_4 through a mild, simple and green process.

In addition, few work was related to the fundamental understanding of the effect of conjugation degree and delocalized π-system on the photocatalytic activity of single layer g-C_3N_4. Though the conjugation degree and delocalized π-system can be regulated by using different precursors and reaction temperature, but the roles of them in photocatalytic reaction are still unclear [12,13]. The enhancement of photocatalytic performance was simply ascribed to the high specific surface area, proper vacancy or compact planar structure. The importance of conjugation degree and delocalized π-system was neglected. It is still a great demand to investigate the relationship of conjugation degree/delocalized π-system and photocatalytic activity in such single layer g-C_3N_4.

In this work, we report that a new atomic single layer g-C_3N_4 with extended planarized structure has been developed successfully by a sandwich-like orientation growth of melamine (MA) and polyacrylamide (PAM). In the traditional bottom-up method, anchoring asymmetric benzene-like organic molecules into the planar edge through the copolymerization process damaged the growth of g-C_3N_4 [14–16]. However, according to the tunable surface electrical behavior and favorable adsorption ability of PAM [17], the orientation growth of MA will occur instead of disordered condensation to pristine g-C_3N_4. Then, it is easy to remove the inserted PAM completely from the layer-stacked sample [18].

Since the increase of free charge carriers generated in ultrathin planarized conjugation system, these two kinds of atomic layer g-C_3N_4 nanosheets have the potential to be an ideal visible light driven photocatalysts. In this paper, we report and compare the

photocatalytic activities of g-C_3N_4 controlled by PAM and acid exfoliation one under visible light irradiation. The aim of this study is to improve the photocatalytic activity of pristine g-C_3N_4 without any other modification, focusing on promoting light energy utilization. The differences of conjugation degree and delocalized π-system in these two atomic single layer g-C_3N_4 samples will be investigated and their effects on the photocatalytic activity will also be discussed.

2. Experimental

2.1. Preparation of g-C_3N_4-PAM, g-C_3N_4-H_2SO_4, and pristine g-C_3N_4

All of the reagents were purchased from Aladdin (Shanghai, China) and used as received without further purification.

The g-C_3N_4-PAM was prepared by directly heating the mixture of melamine (MA) and polyacrylamide (PAM) in an alumina crucible in a muffle furnace. Typically, 0.50 g of PAM and 5.00 g of melamine were well dispersed in 1 L of deionized water under stirring for 2 h. The white precipitation was separated by centrifugation and dried at 60 °C for 24 h. Then the light brown g-C_3N_4-PAM powder was obtained after heating the dried precipitation at 550 °C temperature for 3 h.

The g-C_3N_4-H_2SO_4 nanosheets were synthesized through a harsh lewis acid treatment [5,6]. Typically, 1 g of pristine g-C_3N_4 was dispersed in 5 mL of concentrated H_2SO_4 for 24 h under magnetic stirring. Then, the final sample was obtained after centrifugation and washing by deionic water for a few times. For comparison, other protonic acids HCl and H_2SO_4/HNO_3, and non-protonic acid $(Ac)_2O$ were also chosen to fabricate g-C_3N_4 nanosheets by exfoliation of the pristine one, respectively.

The pristine g-C_3N_4 was synthesized by the thermal polycondensation of melamine without adding PAM [19]. For comparison, N-doped TiO_2 powders with anatase phase structure were also prepared [20].

2.2. Characterization

X-ray diffraction (XRD) characterizations were performed on a Shimadzu XRD-6000 powder X-ray diffractometer with CuKa radiation. The FT-IR spectra were recorded using a VERTEX 70 V/80 V Fourier transformed infrared spectrometer (Bruker, Germany) by means of the KBr pellet technique. X-ray photoelectron spectroscopy (XPS) measurement was done using a Kratos AXIS Ultra DLD XPS system with a monochromatic AlKα source and a charge neutralizer, all the binding energies were referenced to the C1s peak at 284.6 eV of the surface adventitious carbon. The amounts of carbon, nitrogen and oxygen in different g-C_3N_4 were determined by an oxygen-nitrogen-carbon ananlyzer (Elementar, Vario EL). Atomic force microscopy (AFM) study in the present work was performed by Agilent 5500 ILM. The UV/VIS diffuse reflectance spectra were obtained on a Perkin-Elmer Lambda 950 UV/Vis spectrometer equipped with Labsphere integrating over the spectral range of 190–900 nm. The Transmission electron microscopy (TEM) and high-resolution TEM (HRTEM) images were obtained with a JEOL JEM-2100 microscope. The photoluminescence (PL) spectra were obtained on an FLS-920T fluorescence spectrophotometer. The excitation wavelength was 280 nm. Both of the width for excitation and emission slits was 3 nm. The specific surface areas were measured out by the BET method (Micromeritics Instrumetns, TriStar α3020). Electron paramagnetic resonance (EPR) spectra were recorded with a Bruker A300-9.5/12 at 100 kHz field modulation in the standard TE102 regular cavity using thin-walled quartz EPR tubes (Bruker). First, the as-prepared g-C_3N_4 powders were dispersed in methanol using EMXplus X-band spectrometer (Bruker). Then, the g-C_3N_4 suspension (5 g L^{-1}) and DMPO methanol solution (100 mg L^{-1}) were mixed with equal volume. The mixed solution was irradiated by visible light using a 3 W visible light LED (Li Ang, China) lamp (400–750 nm) with 9.4 mW/cm^2 intensity at 298 K for 5 min before every recording. The microwave frequency and power were 9.447 GHz and 24.103 mW. The measurement at a centre field was of 3362 G. The time constant is 40.96 ms and the sweep time is 75 s. Electron spinning resonance (ESR) was measured by JES-FA300. The particle size distribution was analyzed in water solution via Dynamic light scattering measurement (DLS) with a BI-200SM laser light scattering instrument. Photocurrents were measured using an electrochemical analyzer (CHI 660b) in a standard three-electrode system using the prepared samples as the working electrodes with an active area of ca. 1.00 cm × 1.00 cm, a Pt foil and an Ag/AgCl (saturated KCl) electrode were used as the counter electrode and reference electrode, respectively. A 0.1 M Na_2SO_4 solution was used as the electrolyte. A 500 W Xe lamp with intensity of 43 mW/cm^2 was served as a visible light source. Working electrodes were prepared according to our previous work [19]. The electrochemical impedance spectroscopy (EIS) was measured at −1.4 V (vs. RHE) in 0.5 M Na_2SO_4 solution, and the perturbation signal was 5 mV with the frequency ranged from 0.1 Hz to 100 kHz.

2.3. Photocatalytic activity evaluation

Organic pollutants degradation: The photocatalytic activities of samples were investigated by evaluation the decomposition of different organic pollutants aqueous solutions. First, a volume of 50 mL of aqueous solution with 10 mg/L initial concentrations of methylene blue (MB), methyl orange (MO), or Rhodamine B (RhB) dyes was stirred in the dark in presence of as-prepared g-C_3N_4 photocatalyst at a concentration equal to 0.5 g/L. After 30 min to reach the adsorption equilibrium, a compositive LED lamp with 100.3 mW/cm^2 intensity was employed for visible light irradiation source to induce the photocatalysis reaction. Then, samples were withdrawn from the reactor at regular time intervals, centrifuged and analyzed in order to monitor the organic pollutants concentration. The visible light photocatalytic activities of samples on the decomposition of 5 mg/L phenol aqueous solution were also studied under the similar condition.

Photocatalytic H_2 evolution: In this photocatalytic activity test, a 3 W visible light LED (Li Ang, China) lamp (9.4 mW/cm^2) with the wavelength from 400 to 750 nm was employed as the light source. Typically, 50 mg of sample was dispersed in an aqueous solution (100 mL) containing 10 mL of the 10 vol.% triethylamine (TEOA) as a sacrificial agent and 5 mg of Eosin Y (EY) as a photosensitizer. Pt (3 wt.%) was loaded on the surface of the photocatalyst as a cocatalyst by the photodeposition of H_2PtCl_6. Prior to irradiation, the reaction solution was sealed by a silicone stopper, and subsequently flushed with dry nitrogen to remove air, and sonicated for ~1–2 min in dark to guarantee an adsorption-desorption equilibrium between the photocatalyst and reactant. A calibrated Varian GC-3380 Gas Chromatograph equipped with a thermal conductivity detector was employed to determine the evolved hydrogen, using nitrogen as the carrier gas.

The apparent quantum yield (AQY) for the H_2 evolution was determined by using the same 3 W visible light LED (Li Ang, China) lamp as light source. The AQY was calculated as

$$AQY = \frac{n \times N(H_2)}{N_p} \times 100\% \tag{21}$$

where the electron factor n of the reaction $(2H^+ + 2e^- \rightarrow H_2)$ is 2, N_e is the amount of produced H_2 molecules, and N_p is the amount of incident photons.
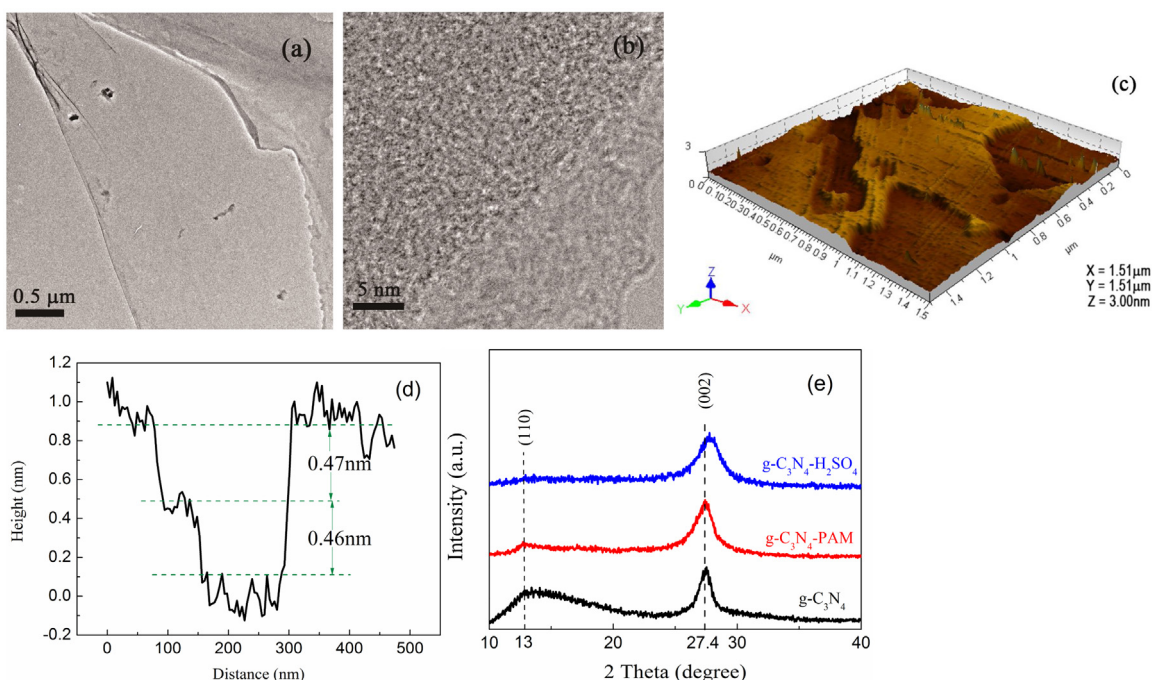
Fig. 1. (a) TEM, (b) HRTEM, and (c) AFM images of g-C$_3$N$_4$-PAM. (d) The corresponding height image of two random nanosheets. (e) XRD patterns of g-C$_3$N$_4$-PAM, g-C$_3$N$_4$-H$_2$SO$_4$ and pristine one.

2.4. Investigation on the generation of $\bullet O^{2-}$, $\bullet OH$, and h^+ radicals

To investigate the active species generated in the photocatalytic degradation process, the experiments of active species (hydroxyl radical ($\bullet$OH), hole (h^+) and $\bullet O^{2-}$) capture were carried out by using 5.0 mg of isopropyl alcohol, ammonium oxalate or benzoquinone under the same visible light irradiation, respectively (as shown in Table S2). The active species in the visible light photocatalytic process of RhB dyes decomposition were detected through trapping experiments of radicals and holes by these scavengers.

2.5. Theoretical calculation

The calculations about melamine and PAM were performed by using Gaussian09 program at the density functional B3LYP level using the 6–31g(d) basis set for both geometry optimization and frequency calculation.

3. Results and discussion

By heat of the mixture of melamine and PAM powders with designed amount ratio at 550 °C in air for 3 h, a light brown powder sample is obtained.

Transmission electron microscopy (TEM) was used to investigate the morphology and microstructure of g-C$_3$N$_4$-PAM. As shown in Fig. 1a, the g-C$_3$N$_4$-PAM exhibits a ultrathin layer structure with a negligible quantity of small particles. The HRTEM image (Fig. 1b) of the sample displays layer structure with some chiffon-like ripples and wrinkles. The thickness of the nanosheets was further confirmed by AFM analysis. As shown in Fig. 1c and d, the randomly measured nanosheets are of the thickness from ca. 0.46 nm to ca. 0.93 nm, indicating the exfoliated nanosheets are composed of only one or two stack layers. Another ultrathin nanosheet one was also obtained via an efficient acid treatment for comparison. X-Ray Diffraction (XRD) analysis was carried out to investigate the crystal structure of the samples. Fig. 1e displays the XRD patterns of pristine g-C$_3$N$_4$, g-C$_3$N$_4$-PAM and g-C$_3$N$_4$-H$_2$SO$_4$ samples. It shows that

all g-C$_3$N$_4$ samples have two characteristic peaks. A dominant peak at 27.4° relates to the (002) plane, which is owing to the interlayer distance d = 0.324 nm in pristine g-C$_3$N$_4$ (Table S1). A small diffraction peak at 13° corresponds to tri-s-triazine units and is indexed as the (110) plane according to JCPDS 87-1526 [19]. No impurity peak was observed. Remarkably, the peak at 13° becomes much weaker in g-C$_3$N$_4$-PAM and even disappears in g-C$_3$N$_4$-H$_2$SO$_4$, owing to the layer exfoliation. Considering the steric and electrostatic effect of PAM polymers, with an amount of functional groups in the molecular chain, it is easy to link with MA by non-covalent bonds through the interaction of acyl-oxygen and amino groups. The combination of PAM and tri-s-triazine units will restrict the layers overlapping of g-C$_3$N$_4$. Therefore, atomic single layer g-C$_3$N$_4$ has been prepared successfully by this facile method.

First, the photocatalytic activities of two kinds of single layer g-C$_3$N$_4$ and pristine one have been evaluated under visible light irradiation. Interestingly, as the same ultrathin atomic layer nanosheets, g-C$_3$N$_4$-PAM and g-C$_3$N$_4$-H$_2$SO$_4$ show quite different photocatalytic selectivity on organic pollutant degradation. As shown in Fig. 2a, g-C$_3$N$_4$-PAM has an advantage on photocatalytic MB dye decomposition while g-C$_3$N$_4$-H$_2$SO$_4$ degrades MO dye in a shorter time. N-TiO$_2$ can finish the removal of MB dye prior to RhB or MO dye similar to g-C$_3$N$_4$-PAM. For more details, see Fig. S1. To further investigate the photocatalytic selectivity, two different surfactants were added into the photocatalytic reaction system respectively. Especially, cetyltrimethyl ammonium bromide (CTAB) is a typical cationic surfactant while sodium dodecyl sulfate (SDS) is an anionic one. As shown in Fig. 2b and c, an improvement of degradation efficiency is observed in both CTAB-CN-PAM-MO and SDS-HS-CN-MB system. But, the photocatalytic degradation reaction would not be promoted if the addition of CTAB and SDS was reversed. N-TiO$_2$, a negative photocatalyst, prefers to decompose of positive MB with better adsorption rather than removal anionic MO [22]. The surface of g-C$_3$N$_4$-PAM should be negative like N-TiO$_2$. It is also reported that under acidic conditions, the protonation of amino groups will make for the positive surface of g-C$_3$N$_4$ [23]. The above results suggest that the surface
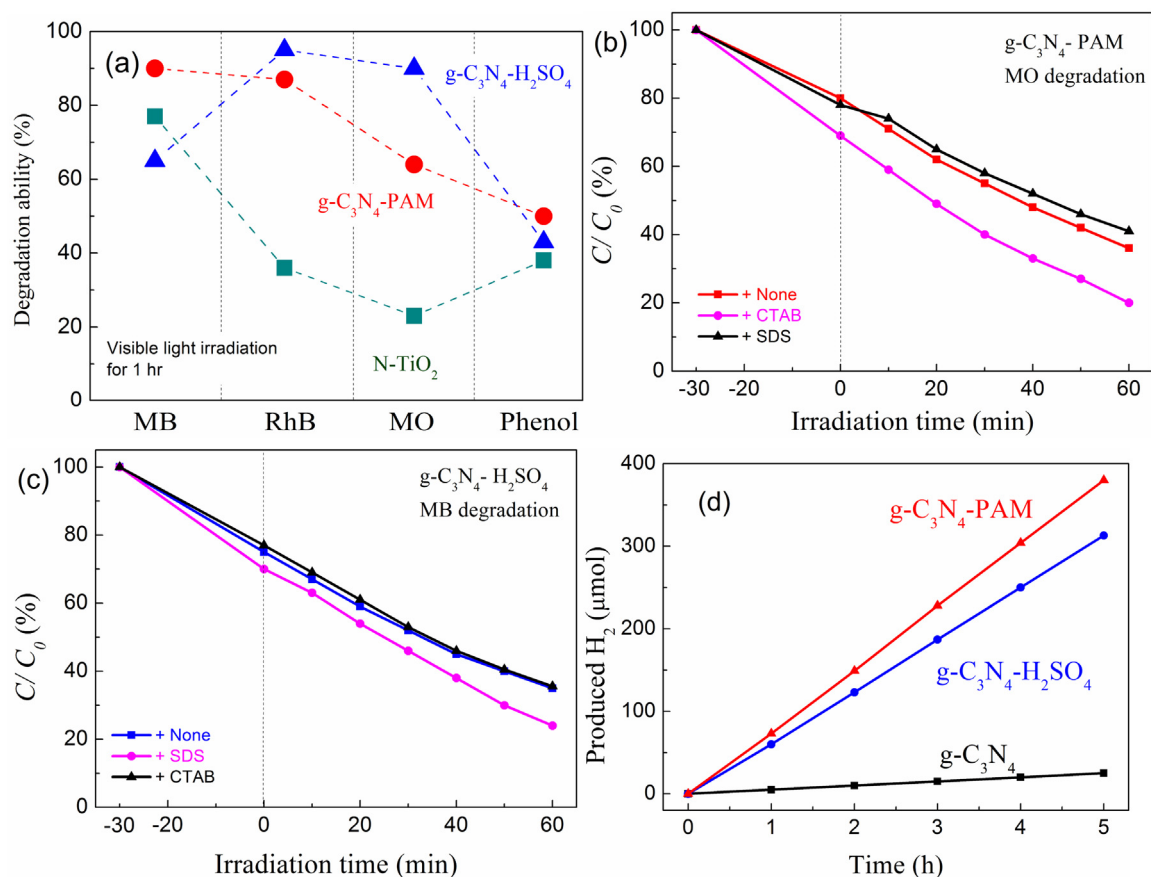
Fig. 2. Photocatalytic activities on (a) organic pollutants degradation, (b) MO, (c) MB degradation adding CTAB or SDS, and (d) H_2 production over different g-C_3N_4 under visible light irradiation.

electricity of g-C_3N_4 has been changed after chemical exfoliation. This change may proceed along with the partial destruction of g-C_3N_4. On the contrary, PAM does not harm the g-C_3N_4. In addition, on the neutral phenol decomposition, g-C_3N_4-PAM possess a little better photocatalytic activity than other two g-C_3N_4 samples (Fig. 2a).

Photoinduced charge carriers separation and transfer are essential to the photocatalytic reaction process. Photocatalytic water splitting was carried out to demonstrate the ability of charge separation and transfer. In this hydrogen evolution studies, three different reagents were used, i.e. TEOA as a sacrifice reagent, Eosin Y as a photosensitizer and deposited Pt as a cocatalyst. As shown in Fig. 2d, g-C_3N_4-PAM exhibits a higher photocatalytic activity than g-C_3N_4-H_2SO_4 using visible light irradiation under the same reaction conditions. The average hydrogen production rate (HER) of g-C_3N_4-PAM reached 76 μmol/h higher than that of g-C_3N_4-H_2SO_4 (62 μmol/h). The AQY of the photocatalytic hydrogen evolution was determined to be 1.1% for g-C_3N_4-PAM and 0.8% for g-C_3N_4-H_2SO_4 in the whole visible light spectrum. It is well known that the photocatalytic performance is highly influenced by surface area, light harvest ability, charge separation and mobility. As shown in Table S1, both samples exhibit similar surface areas (31.46 and 35.27 m^2/g), which are higher than that of pristine g-C_3N_4 material (15.97 m^2/g). Since g-C_3N_4-PAM exhibits a H_2 evolution 1.2 times better than that of g-C_3N_4-H_2SO_4 under visible light irradiation, but the light absorption ability and surface area are common, light absorption and surface area are not the key point in the differences over photocatalytic performance. It suggests that g-C_3N_4-PAM is superior to g-C_3N_4-H_2SO_4, which may be owing to the better charge separation and transfer.

To further illuminate the failure of g-C_3N_4-H_2SO_4, different concentrated acids have been chosen to prepare samples. The pristine g-C_3N_4 was treated by protonic acid, e.g., HCl and HNO_3/H_2SO_4, and non-protonic acid (Ac)$_2$O respectively. As presented in Fig. S2, after protonic acid treatment, the (110) peak at 13.0° disappears, clearly indicating that g-C_3N_4 samples is well exfoliated to form layered structure. However, the (Ac)$_2$O-g-C_3N_4 one still exhibits a weak (110) peak owing to the weak exfoliation performance. TEM images of pristine g-C_3N_4 and acid exfoliation ones are shown in Fig. S3. The pristine g-C_3N_4 exhibits the typical overlap platelet-like surface morphology that changes to a thin and small nanostructure after H_2SO_4 and HCl treatment, suggesting the protonation exfoliation. But, no clear differences have been observed between the morphology of (Ac)$_2$O-g-C_3N_4 and pristine one. The different results suggest that the protonation is of great importance to form single layer by the complete destruction of interlayer van der waals force.

Then, the investigation of the electronic band structure of the g-C_3N_4-H_2SO_4, g-C_3N_4-HCl, and g-C_3N_4-H_2SO_4-HNO_3 by a combined analysis of the Mott-Schottky plots and UV–vis absorption spectrum was carried out. As shown in Fig. S4, the intrinsic absorption edge of protonic acid-g-C_3N_4 shows great blue shift while that of the nonprotonic acid-one has slight red shift in comparison with the pristine one, and the band gap of g-C_3N_4-HCl of ca. 3.02 eV increases to 3.07 and 3.10 eV for g-C_3N_4-H_2SO_4 and g-C_3N_4-H_2SO_4-HNO_3 while that of (Ac)$_2$O-g-C_3N_4 one is ca. 2.77 eV. And in the meantime, the absorption abilities of protonic acid-g-C_3N_4 and nonprotonic acid-one increase in the visible and UV light region respectively, which should be ascribed to the improved interlayer separation and decrease of particle size. As a result, g-C_3N_4-H_2SO_4
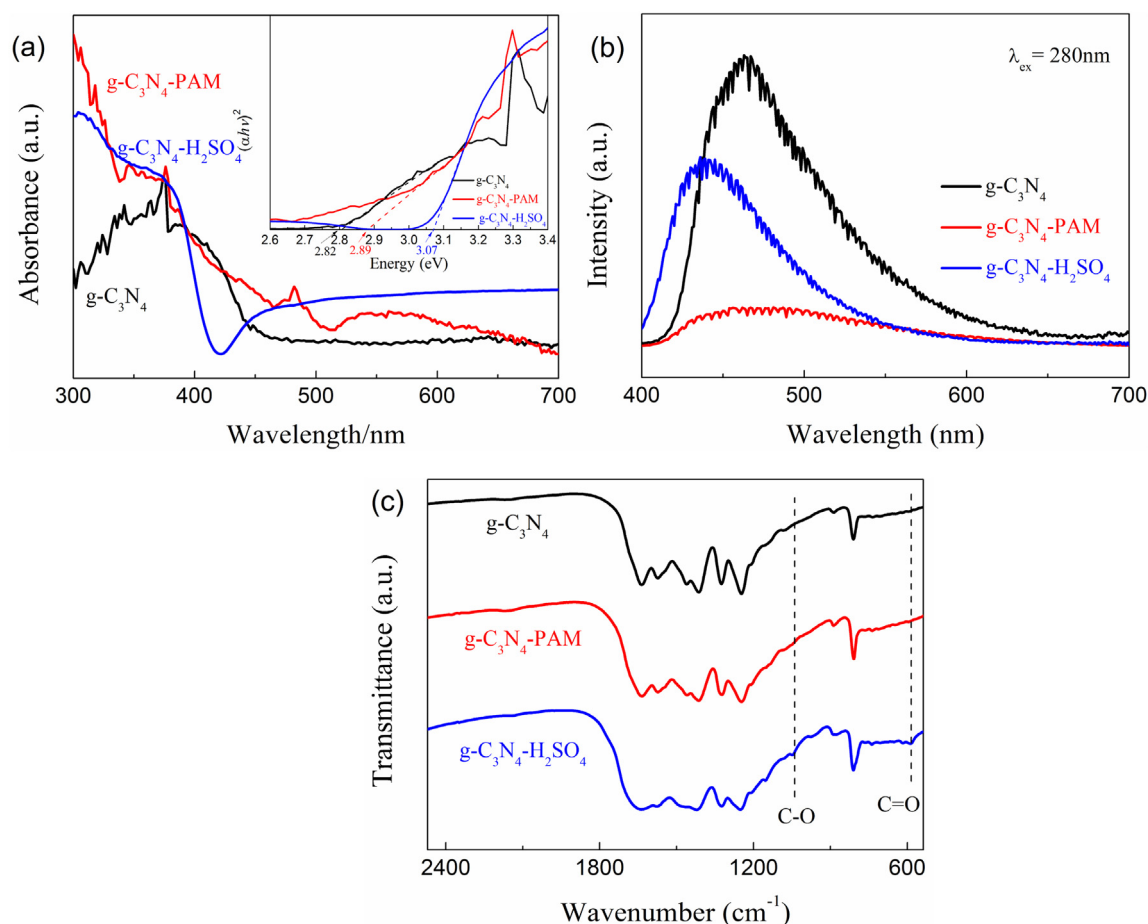
Fig. 3. (a) UV–vis absorption spectra of g-C$_3$N$_4$-PAM, g-C$_3$N$_4$-H$_2$SO$_4$ and pristine one and the corresponding Tauc plot (inset). (b) PL and (c) FTIR spectra of different g-C$_3$N$_4$ samples.

has been chosen for further investigation. To explain the superiority of g-C$_3$N$_4$-PAM on visible light driven photocatalytic ability, some other characterizations, such as DRS, FTIR and elements analysis, were carried out.

Both g-C$_3$N$_4$-PAM and g-C$_3$N$_4$-H$_2$SO$_4$ exhibit the typical absorption curves of semiconductors, as shown in Fig. 3a. The band gap energy of g-C$_3$N$_4$-PAM is 2.89 eV much lower than that of g-C$_3$N$_4$-H$_2$SO$_4$ (3.07 eV). The narrower band gap may make g-C$_3$N$_4$-PAM capture more photons to generate free charges [24].

The photoluminescence spectrum was used to further evaluate the ability of charge transition and separation [25]. As shown in Fig. 3b, it shows a broad and strong photoluminescence at about 460 nm, which is attributed to the recombination process of self-trapped excitation [26]. For pristine g-C$_3$N$_4$, the overlapped layers structure goes against the separation of electrons and holes, which would lead to the strong PL emission. The luminescence becomes much weaker in g-C$_3$N$_4$-PAM, indicating the improvement of charge localization on the surface terminal sites, which is believed to promote the photocatalytic redox functions. This well-confined electrons-holes separation also illustrates the single atomic layer structure. However, only a blue shift is observed for the PL of g-C$_3$N$_4$-H$_2$SO$_4$ with a decreased intensity. For the reason, the oppositely move of the conduction and valence band edges caused by the quantum confinement effect results in the larger band gap and blueshift of the PL spectrum [27]. The results suggest that the charge carriers can not be as free in g-C$_3$N$_4$-H$_2$SO$_4$ as in g-C$_3$N$_4$-PAM.

In addition, in Fig. S5, the PL spectra of not only g-C$_3$N$_4$-H$_2$SO$_4$ but also g-C$_3$N$_4$-HCl, and g-C$_3$N$_4$-H$_2$SO$_4$-HNO$_3$ have blue shift, which are quite different from g-C$_3$N$_4$-PAM. Among them, g-C$_3$N$_4$-H$_2$SO$_4$-HNO$_3$ may be expected to possess better electrons-holes separation ability than other two since the lower intensity of PL. However, the large band gap (3.10 eV) prevents g-C$_3$N$_4$-H$_2$SO$_4$-HNO$_3$ from being a visible light driven photocatalyst. Although the intensity of PL peak for (Ac)$_2$O-g-C$_3$N$_4$ decreases, it does not shift and (Ac)$_2$O-g-C$_3$N$_4$ is not of single atomic layer structure.

Fig. 3c shows the FTIR of the g-C$_3$N$_4$-PAM, g-C$_3$N$_4$-H$_2$SO$_4$ and pristine g-C$_3$N$_4$ samples. The strong band peak between 1700 and 1200 cm^{-1}, with the characteristic peaks at 1247, 1326, 1417, 1463, and 1571 cm^{-1}, are the characteristic stretching vibration of C—N and C=N heterocycles, and the peak at 810 and 1636 cm^{-1} is the breathing mode of s-trizaine ring units. [28] It can be clearly seen that the main absorption peaks of g-C$_3$N$_4$ appear without impurity peaks except two foreigner peaks in the spectra of g-C$_3$N$_4$-H$_2$SO$_4$. One peak at 1040 cm^{-1} is ascribed to the stretching of C—O, another at 586 cm^{-1} is caused by C=O bond [27]. The formation of oxybond occurred in g-C$_3$N$_4$ after protonic acid treatment. In addition, some peaks of CN bonds in g-C$_3$N$_4$-H$_2$SO$_4$ became dramatic weak, i.e. the peaks at 1414, 1484, and 1574 cm^{-1}, indicating the partial destruction of CN bonds and the loss of C or N atoms.

The O doping may also cause the wideness of band gap in g-C$_3$N$_4$-H$_2$SO$_4$, which results in a blueshift of the absorption edge (Fig. 3a) [27]. It is no doubt that the destruction of CN bonds will result in a lower degree of conjugation. The g-C$_3$N$_4$-PAM that shows a higher degree of conjugation is more active than the protonic
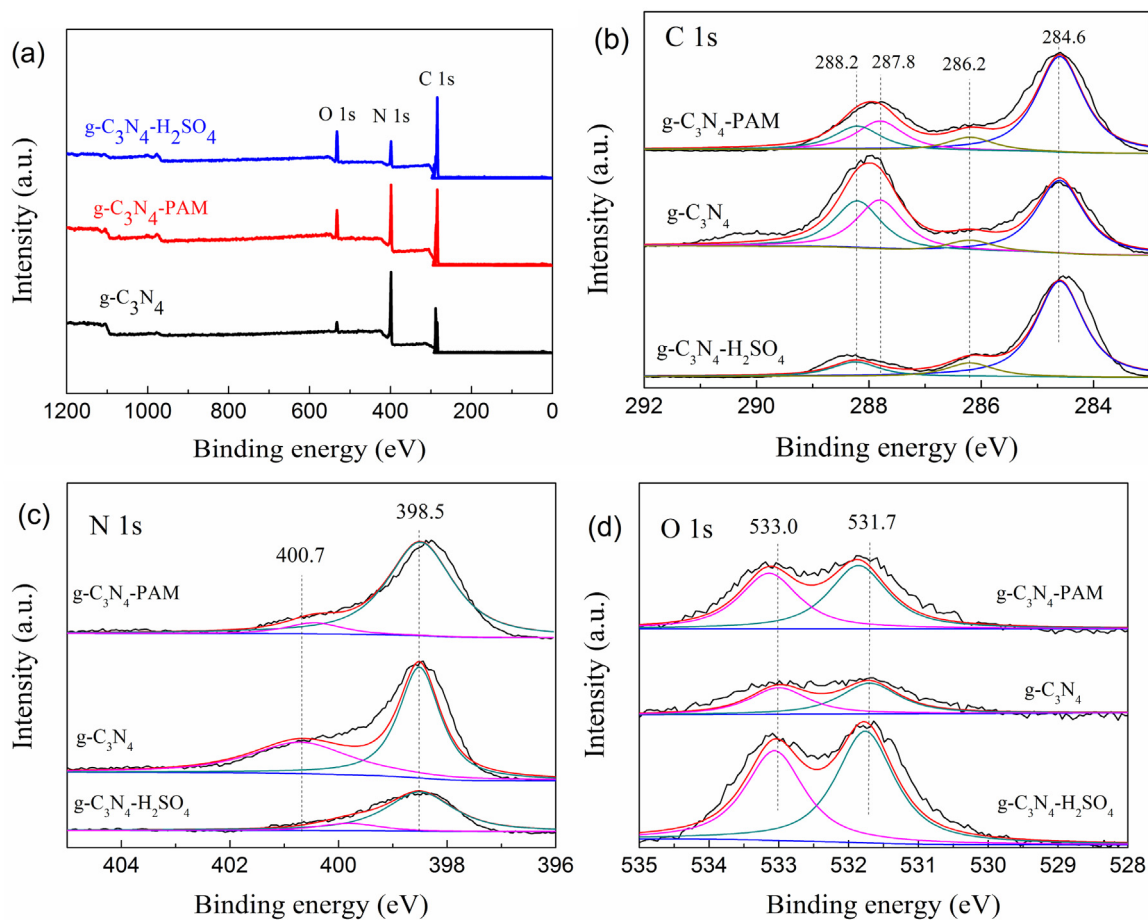
Fig. 4. XPS results of (a) the survey spectra and high-resolution spectra of (b) C 1s, (c) N 1s, and (d) O 1s for different g-C_3N_4 samples.

acid treated one under light irradiation. This outcome is due to the decreased band gap that contributes to the capture of more photons for the generation of more excited charge carriers [24].

The chemical states of single layer g-C_3N_4 and the pristine one were studied by XPS (Fig. 4). As shown in Fig. 4a, all samples show three sharp peaks ascribing to C1s, N1s and O1s respectively. In the C1s spectra, the peaks at 287.8 and 288.2 eV are indexed to the sp^2 hybridized carbon in the CN and C−N═C bonds respectively, while the peaks at 398.5 and 400.7 eV are attributed to the sp^2-bonded N in C−N═C and the bridging N atoms in N-(C)$_3$ or N−H in the N1s spectra respectively, in Fig. 4b–c. The lowest peak at 286.2 eV is attributed to the C−NH$_2$ species [29]. The peak at 404.2 eV in the N1s spectra corresponds to the positive charge localization in heptazine rings [27]. In Fig. 4d, the O 1s spectra of all g-C_3N_4 are fitted into two peaks, ca. 533.0 eV attributing to the adsorbed H$_2$O and ca. 531.7 eV owing to the surface hydroxyl group [30]. The more exposed surface in single atomic layer g-C_3N_4-PAM can adsorb more H$_2$O and −OH groups, which results in the higher intensity than that of pristine g-C_3N_4. However, besides the surface adsorption, the extra increase in the peak intensity may be caused by the possible presence of oxy-functional groups in the g-C_3N_4-H$_2$SO$_4$.

The partial oxidation of CN has been confirmed by the above results of FTIR. Compared with pristine g-C_3N_4, the peaks of C1s and N1s shift or even disappear and the peaks of O1s increases sharply in the g-C_3N_4-H$_2$SO$_4$ while no obvious change has been observed in the g-C_3N_4-PAM, demonstrating again that the protonic acid breaks the bonds and the triazine rings partially while PAM is friendly to g-C_3N_4. The damage will leave behind a great amount of carbon-rich small fragments on the surface of g-C_3N_4-H$_2$SO$_4$, as shown in TEM image of Fig. S2.

The C/N ratio was calculated by the area ratio of C to N from the C1s and N1s XPS spectra. As listed in Table 1, two kinds of single layer g-C_3N_4 photocatalysts exhibit higher C/N ratio than pristine one and the g-C_3N_4-H$_2$SO$_4$ has the marvelous value, which is confirmed by elements analysis. According to the highest C/N ratio, the surface carbon-rich may improve the photocatalytic activity of g-C_3N_4-H$_2$SO$_4$ by promoting the photogenerated electrons and holes separation [31]. However, as shown in Figs. 2 and S1, the photocatalytic activity of g-C_3N_4-PAM is higher than that of g-C_3N_4-H$_2$SO$_4$. It indicates that the planar extension played a crucial role on the enhancement of photocatalytic ability. From XPS and elements analysis (Table 1), it also confirmed the high amount of oxygen ele-

Table 1
The amount of C, N, and O in different g-C_3N_4 samples.

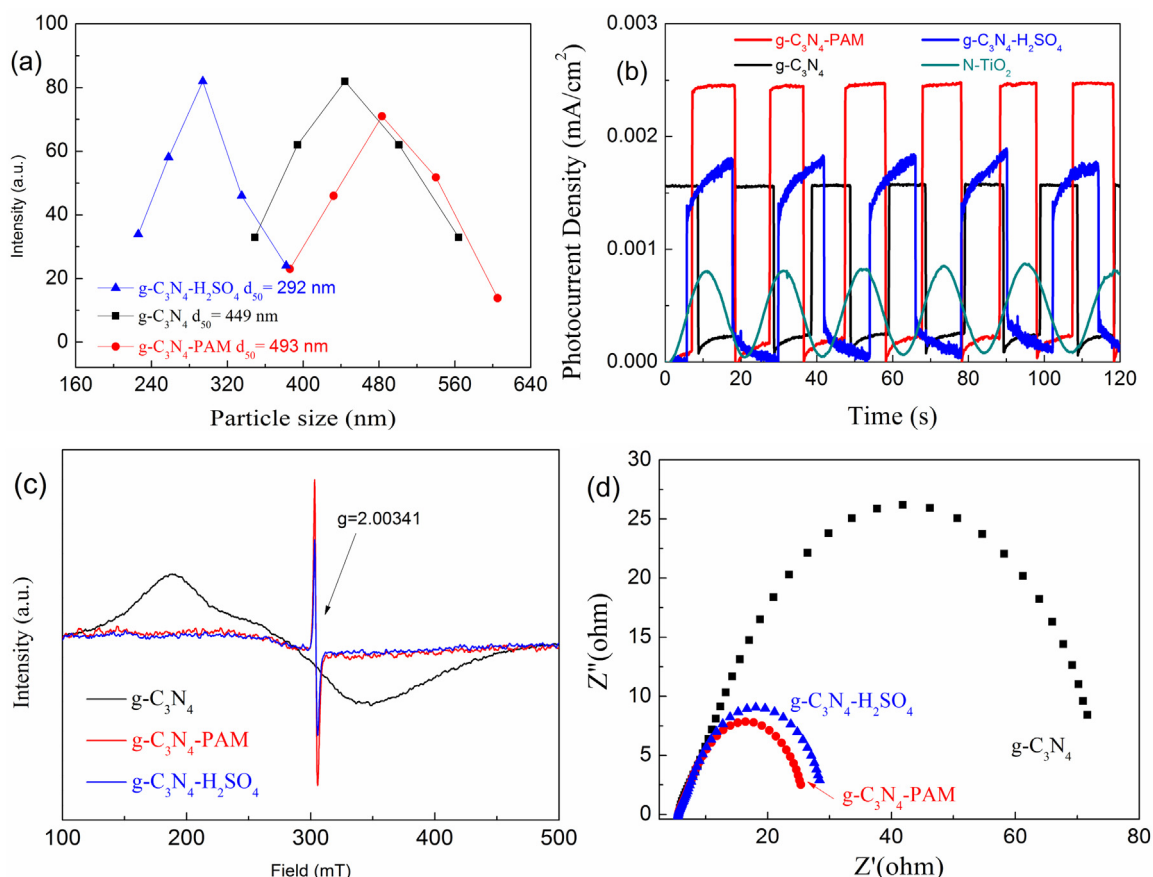| Content (%)	XPS surface elemental analysis				Elemental analysis			
	C	N	O	C/N	C	N	O	C/N
g-C_3N_4	53	43	4	1.23	41.2	53.7	3.9	0.77
g-C_3N_4-PAM	55	39	6	1.41	44.0	49.5	6.4	0.89
g-C_3N_4-H$_2$SO$_4$	62	28	10	2.21	44.0	45.6	10.4	0.96

Fig. 5. (a) Particle size distribution of different g-C$_3$N$_4$. (b) Photocurrent-time dependence of different g-C$_3$N$_4$ samples under visible light irradiation. (c) Comparison of ESR spectra of different g-C$_3$N$_4$ under visible light irradiation. (d) Nyquist impedance plots for different g-C$_3$N$_4$.

ment in g-C$_3$N$_4$-H$_2$SO$_4$, i.e. the O content reached ca. 10%, which was improved by a factor of ~1.7 over that of the g-C$_3$N$_4$-PAM (ca. 6%) and ~2.6 over that of the pristine one (ca. 4%).

In order to determine the size of different g-C$_3$N$_4$, DLS measurement was carried out. As shown in Fig. 5a, the hydrodynamic diameter of g-C$_3$N$_4$-H$_2$SO$_4$ particles is 292 nm much shorter than 493 nm of g-C$_3$N$_4$-PAM and 449 nm of pristine one. It suggest that the concentrated acid exfoliation of pristine g-C$_3$N$_4$ will fabricate a mass of tiny fragments. It well agrees with the result from TEM image of Fig. S2a. On the other hand, the extension of g-C$_3$N$_4$ planar, which can be seen in Fig. 1a, will result in the large particle size. It seems that smaller nanoparticles with more active sites will possess excellent photocatalytic activity. However, the poor interparticle electron transport in the nano-particles results in a low overall conductivity [32].

From the above results in FTIR, the escapement of C or N atoms and the introduction of O atoms after concentrated H$_2$SO$_4$ treatment inevitably cause the formation of doping and defect structure. It tends to aggravate the disorder degree of structure and electrons [33]. Besides, the existence of defect also suppresses the exciton diffusion in the conjugated polymers [34]. For example, Fe doping results in the low intensity of photocurrent peaks in g-C$_3$N$_4$ [21]. The result of all these various matters is the low conductivity. Since the weak conductivity, the charge transfer mainly occurs between nearest neighbor molecules or within a short distance.

The photocurrent responses of g-C$_3$N$_4$-PAM, g-C$_3$N$_4$-H$_2$SO$_4$, and g-C$_3$N$_4$ on the FTO conductive glass under visible light irradiation were evaluated to further offer information for the separation and transfer efficiency of photogenerated electrons and holes. The transient photocurrent responses of all g-C$_3$N$_4$ photocatalysts at light

on and light off are reversible and stable, as shown in Fig. 5b. The photocurrent of g-C$_3$N$_4$-PAM is much higher (2.5 µA/cm^2) than that of g-C$_3$N$_4$-H$_2$SO$_4$ (1.8 µA/cm^2) and pristine one (1.6 µA/cm^2). The improvement occurred after PAM addition indicates that single atomic layer structure of g-C$_3$N$_4$ is formed with large planar, which promotes the separation of photogenerated charge carriers and therefore an excellent visible light photocatalytic performance is obtained. It has been confirmed that the low overall conductivity will reduce the total photocatalytic activity.

One of the main differences between g-C$_3$N$_4$-PAM and g-C$_3$N$_4$-H$_2$SO$_4$ is the large planarized structure. The delocalized π-system is extended in the large planar g-C$_3$N$_4$-PAM. Unlike inorganic metal oxides photocatalysts, in conjugated polymers, the extension with long molecules will efficiently prolong the distance of electron transport to fight the nature of electron localization [33]. Then, the separation of photo-generated electrons and holes is elevated.

The information about the electronic structure was further studied by solid-state ESR at room temperature. As shown in Fig. 5c, the spectra of the pristine g-C$_3$N$_4$ and two single layer nanosheets are different in patterning but same in the g value. The differences can be attributed to different structural and electrochemical environment in g-C$_3$N$_4$ and g-C$_3$N$_4$-PAM or g-C$_3$N$_4$-H$_2$SO$_4$. Fan et. al reports that the increased EPR signals confirm the enhancement of the delocalization electrons owing to the extend conjugation by aromatic rings incorporation [35]. Thanks to the redistribution of electrons, the single atomic layer g-C$_3$N$_4$ samples present sharp peaks. Other research also suggests that the electron transfer could be extended in a large π conjugate system of conjugated polymers [33]. The stronger sharp peaks reveal that g-C$_3$N$_4$-PAM possesses stronger π-conjugated CN aromatic rings than g-C$_3$N$_4$-H$_2$SO$_4$.
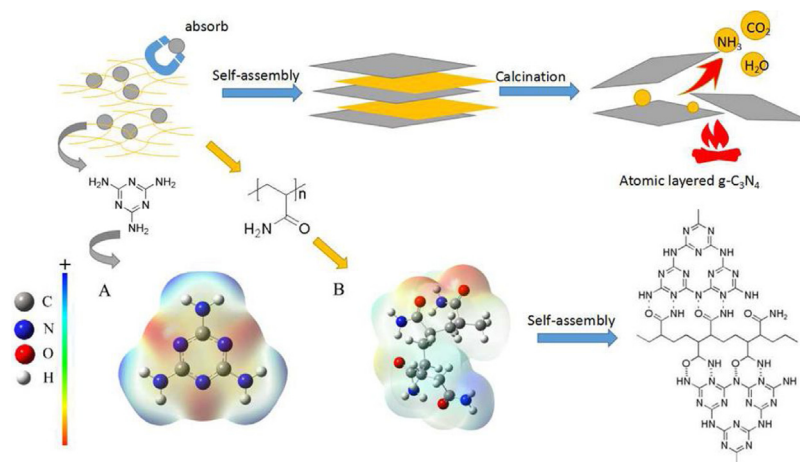
Fig. 6. The diagram of sandwich-like orientation growth for fabrication of atomic layered g-C$_3$N$_4$ by melamine and PAM. A and B exhibit the optimized geometry and charge separation of melamine and PAM, respectively. The color gradation shows the charge polarity, i.e., the white district is on behalf of negative charge, while the black district is the positive one. (For interpretation of the references to color in this figure legend, the reader is referred to the web version of this article.)

Combined with the above results, the charge transfer advantages are from not only the high conjugated degree but also the extended delocalized π-system in the as-prepared g-C$_3$N$_4$-PAM.

As shown in Fig. 5d, according to the semicircle in the low-frequency zone, the charge transfer resistances of g-C$_3$N$_4$, g-C$_3$N$_4$-PAM and g-C$_3$N$_4$-H$_2$SO$_4$ are 74.0, 22.1 and 24.5 Ω respectively, indicating the charge performance is better in g-C$_3$N$_4$-PAM than in g-C$_3$N$_4$-H$_2$SO$_4$.

Different from the partial destruction during chemical exfoliation, single layer g-C$_3$N$_4$ can be fabricated facilely by the self-assembly of MA and PAM. On the basis of the results from the density functional theory (DFT) calculations, for MA and PAM respectively, the N atoms in benzene ring are negative while −NH$_2$ shows positive electrical properties, as shown in Fig. 6(A) and (B). In addition, C=O groups in PAM molecules act as good electron-withdrawing units. It indicates that electron interaction between a negative unit and a positive one is a useful strategy for forming hydrogen bond between MA and PAM. The Cartesian coordinates for each atom in the molecules are listed in the supporting information in more detail. Therefore, the formation mechanism can be related to the molecular assembly structure of MA-PAM as shown in Fig. 6. First, PAM self-assembles to form a textual network with the flexible edge. Melamine self-condenses into tris-s-triazine units with abundant amino groups. The loose PAM textual network can be further linked with tri-s-triazine units by hydrogen bond between acyl-oxygen and amino groups. The generated hydrogen bonds between polymeric layers would gradually extend the layers distance and reduce the layers overlapping. It highly agrees with the other report about non-covalent bond formed in the g-C$_3$N$_4$ photocatalyst [36]. To confirm the hydrogen bond generation, IR analysis was measured. As shown in Fig. S6 and Table S2, 3479, 3430, 1665, and 1446 cm^{-1} in melamine, owing to NH$_2$, C=O, and C−N respectively, shift to the low wavenumber after forming MA-PAM precursor, suggesting the formation of hydrogen bond [23,37].

The g-C$_3$N$_4$-PAM exhibits the specific surface area (S.S.A.) of 31.46 m^2/g 2.0 times larger than pristine g-C$_3$N$_4$ (15.97 m^2/g). The incomplete formation of single layer g-C$_3$N$_4$ would result in a limited increase of specific surface area. The specific surface area of g-C$_3$N$_4$-H$_2$SO$_4$ is 35.27 m^2/g also only 2.2 times than that of pristine one (in Table S3). It should be owing to the incomplete exfoliation by protonation [38]. Anyway, the improved specific surface area of the single layer g-C$_3$N$_4$-PAM will be good for absorbing more active species and reactants on the surface, which should result in a better photocatalytic activity.

The recycling experiments were also performed by RhB decomposition over the g-C$_3$N$_4$-PAM photocatalyst under visible light irradiation. As shown in Fig. 7a, the photocatalytic performance of g-C$_3$N$_4$-PAM does not show a significant decrease after three recycles, indicating the excellent stability. In addition, as shown in Table S3, after three recycles of photocatalytic reaction, both g-C$_3$N$_4$-PAM and g-C$_3$N$_4$-H$_2$SO$_4$ show a slight decrease in specific surface area and a little increase in average particle size, due to the aggregation of nanosheets [39]. No obvious differences has been observed in their FTIR spectra before and after photocatalytic reaction (in Fig. S7). The g-C$_3$N$_4$-PAM exhibits the same results in XRD pattern and UV−vis spectra (in Figs. S8 and S9). On the contrary, the intensity of absorption curve increases in visible light region over g-C$_3$N$_4$-H$_2$SO$_4$ after photocatalytic reaction, though no differences occur in its XRD patterns. The increase is caused by the photosensitized effect of the left RhB on the surface of g-C$_3$N$_4$-H$_2$SO$_4$ [40]. Therefore, not only higher photocatalytic activity, but also better stability is established in g-C$_3$N$_4$-PAM.

To investigate the active species involved in the photocatalytic reaction process, the evaluation was carried out by adding different active radical captures in the 10 mg/L RhB solution over g-C$_3$N$_4$-PAM under visible light irradiation, respectively (Table S4). The experimental results compared with no addition one is shown in Fig. 7b. By inducing •O^{2-} and •OH scavenger into system, benzoquinone and isopropyl alcohol, g-C$_3$N$_4$-PAM exhibits a significant decrease in the photocatalytic activity owing to the less active species to drive the reaction. Conversely, the photocatalytic performance is slightly decreased after adding holes scavenger, EDTA-2Na, indicating that the holes are not the dominant active species. This results imply that both •O^{2-} and •OH generated on g-C$_3$N$_4$-PAM play an important role in RhB decomposition and the •O^{2-} radicals are the main oxidative species.

To further verify the existence of •O^{2-} radicals directly, the electron paramagnetic resonance (EPR) measurement was carried out. In Fig. 7c, DMPO-•O^{2-} signal is clearly observed using methanol as solvent instead of water. Moreover, besides the •O^{2-} signal, impurity signals are also observed, which can be ascribed to the carbon free radicals, similar to g-C$_3$N$_4$ nanorods [41]. The intensity of radical signal for g-C$_3$N$_4$-PAM is obviously stronger than pristine g-C$_3$N$_4$, indicating that the concentration of superoxide radicals in g-C$_3$N$_4$-PAM sample is higher than that of pristine one, which is roughly consistent with the enhanced photocatalytic activity.

Therefore, all the differences between g-C$_3$N$_4$-PAM and g-C$_3$N$_4$-H$_2$SO$_4$ could be summarized. As shown in Table 2, compared with
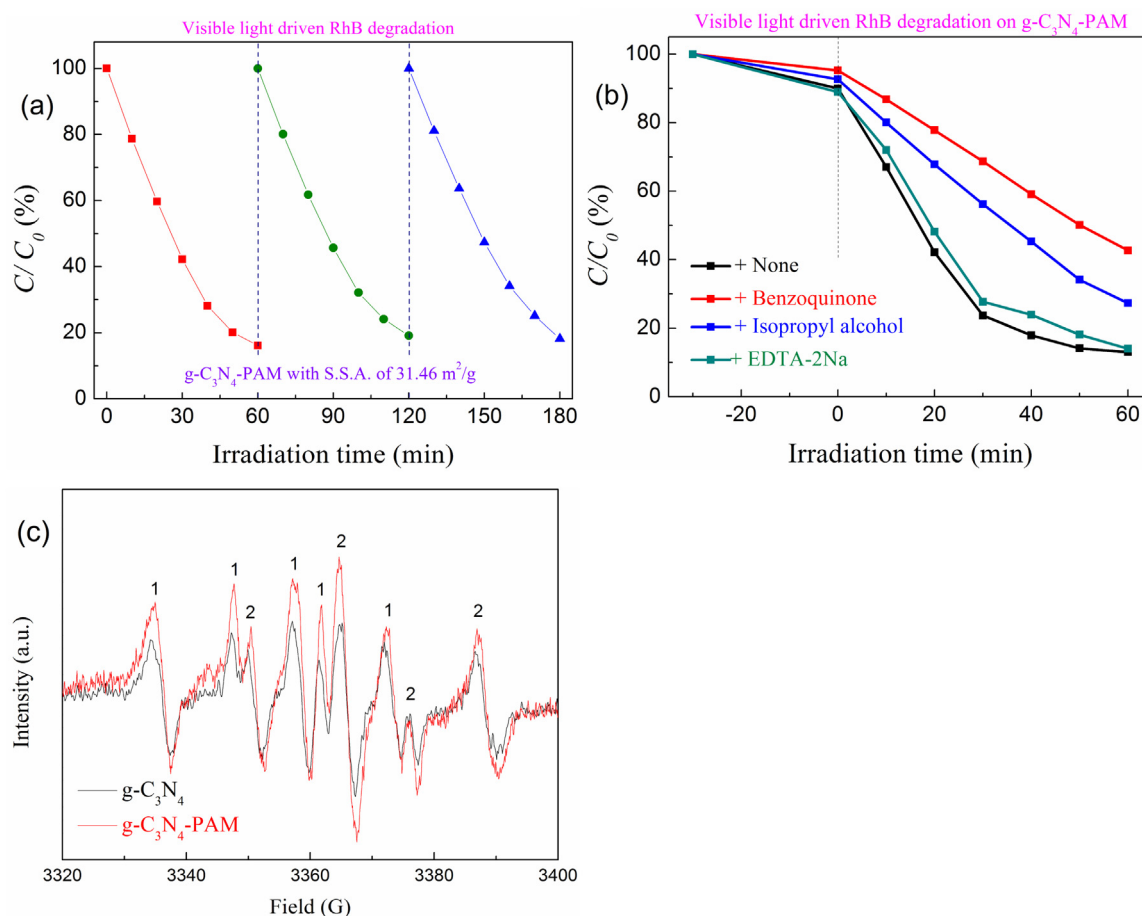
Fig. 7. (a) Circulating runs in the decomposition of RhB over g-C$_3$N$_4$-PAM photocatalyst under visible light irradiation; (b) The plots of the photoinduced carriers trapping in the system of photocatalytic degradation of 10 mg/L RhB over g-C$_3$N$_4$-PAM by adding different active radical captures; (c) DMPO spin-trapping EPR spectra of g-C$_3$N$_4$ and g-C$_3$N$_4$-PAM methanol dispersion for DMPO-$\bullet$O^{2-} (1: DMPO-$\bullet$O^{2-}, 2: carbon free radicals).

Table 2
Differences between g-C$_3$N$_4$-PAM and g-C$_3$N$_4$-H$_2$SO$_4$.

	g-C$_3$N$_4$-PAM	g-C$_3$N$_4$-H$_2$SO$_4$
Sp^2 C—N—C level	high	low
C-NH$_2$ level	low	high
C/N ratio	low	high
Content of O	low	high
O-bonds	None	C—O and C═O
TEM image	Smooth, compact	Rough, porous
Particle size	Large plannar	Small fragments

g-C$_3$N$_4$-H$_2$SO$_4$, g-C$_3$N$_4$-PAM possesses a higher ratio of sp^2 format C—N—C but a lower C-NH$_2$ level and C/N content, indicating a higher conjugate degree. In addition, the protonation posed the obvious existence of defects and destruction of plannar structure, resulting the presence of oxy-bond and increase of O concentration. The differences in TEM image and particle size distribution also reveal the destruction caused by protonation.

4. Conclusions

In summary, different from the pursuit of small nano-particles in inorganic metal oxide photocatalysts, the conjugation degree and the delocalized π-system are two issues of crucial importance for conjugated polymer g-C$_3$N$_4$. Thanks to the maintaining of high conjugation degree, the charge transport is improved by avoiding the aggravation of structural and electronic disorder. In addition, the extension of delocalized π-system will efficiently prolong the distance of electron transport, resulting in the enhanced separation of photo-generated electrons and holes. Our studies indicate that single atomic layer g-C$_3$N$_4$ with high visible light induced photocatalytic activity, even better than N-doped TiO$_2$, can be obtained without the destruction of planarized structure. Akin to the production of sandwich, the orientation growth of g-C$_3$N$_4$ is controlled by PAM in a facile method. The kept conjugation degree and the extended delocalized π-system make g-C$_3$N$_4$-PAM be a promising photocatalyst.

Appendix A. Supplementary data

Supplementary data associated with this article can be found, in the online version, at http://dx.doi.org/10.1016/j.apcatb.2017.06.017.

References

[1] X. Zhang, X. Xie, H. Wang, J. Zhang, B. Pan, Y. Xie, Enhanced photoresponsive ultrathin graphitic-phase C_3N_4 nanosheets for bioimaging, J. Am. Chem. Soc. 135 (2013) 18–21.

[2] S. Yang, Y. Gong, J. Zhang, L. Zhan, L. Ma, Z. Fang, R. Vajtai, X. Wang, P.M. Ajayan, Exfoliated graphitic carbon nitride nanosheets as efficient catalysts for hydrogen evolution under visible light, Adv. Mater. 25 (2013) 2452–2456.

[3] H. Wang, Y. Su, H. Zhao, H. Yu, S. Chen, Y. Zhang, X. Quan, Photocatalytic oxidation of aqueous ammonia using atomic single layer graphitic-C_3N_4, Environ. Sci. Technol. 48 (2014) 11984–11990.

[4] H. Zhao, H. Yu, X. Quan, S. Chen, Y. Zhang, H. Zhao, H. Wang, Fabrication of atomic single layer graphitic-C3N4 and its high performance of photocatalytic disinfection under visible light irradiation, Appl. Catal. B: Environ. 152–153 (2014) 46–50.

[5] J. Xu, L. Zhang, R. Shi, Y. Zhu, Chemical exfoliation of graphitic carbon nitride for efficient heterogeneous photocatalysis, J. Mater. Chem. A 1 (2013) 14766–14772.

[6] X. Zhang, H. Wang, H. Wang, Q. Zhang, J. Xie, Y. Tian, J. Wang, Y. Xie, Single-layered graphitic-C_3N_4 quantum dots for two-photon fluorescence imaging of cellular nucleus, Adv. Mater. 26 (2014) 4438–4443.

[7] P. Niu, L. Zhang, G. Liu, H.M. Cheng, Graphene-like carbon nitride nanosheets for improved photocatalytic activities, Adv. Funct. Mater. 22 (2012) 4763–4770.

[8] Z. Lin, X. Wang, Nanostructure engineering and doping of conjugated carbon nitride semiconductors for hydrogen photosynthesis, Angew. Chem. Int. Ed. 52 (2013) 1735–1738.

[9] J. Zhang, J. Sun, K. Maeda, K. Domen, P. Liu, M. Antonietti, X. Fu, X. Wang, Sulfur-mediated synthesis of carbon nitride: band-gap engineering and improved functions for photocatalysis, Energy Environ. Sci. 4 (2011) 675–678.

[10] J. Liu, T. Zhang, Z. Wang, G. Dawson, W. Chen, Simple pyrolysis of urea into graphitic carbon nitride with recyclable adsorption and photocatalytic activity, J. Mater. Chem. 21 (2011) 14398–14401.

[11] G. Zhang, J. Zhang, M. Zhang, X. Wang, Polycondensation of thiourea into carbon nitride semiconductors as visible light photocatalysts, J. Mater. Chem. 22 (2012) 8083–8091.

[12] M. Caux, F. Fina, J.T.S. Irvine, H. Idriss, R. Howe, Impact of the annealing temperature on Pt/g-C_3N_4 structure, activity and selectivity between photodegradation and water splitting, Catal. Today 287 (2017) 182–188.

[13] H. Lan, L. Li, X. An, F. Liu, C. Chen, H. Liu, J. Qu, Microstructure of carbon nitride affecting synergetic photocatalytic activity: hydrogen bonds vs. structural defects, Appl. Catal. B: Environ. 204 (2017) 49–57.

[14] M. Zhang, X. Wang, Two dimensional conjugated polymers with enhanced optical absorption and charge separation for photocatalytic hydrogen evolution, Energy Environ. Sci. 7 (2014) 1902–1906.

[15] J. Zhang, G. Zhang, X. Chen, S. Lin, L. Mohlmann, G. Dolega, G. Lipner, M. Antonietti, S. Blechert, X. Wang, Co-monomer control of carbon nitride semiconductors to optimize hydrogen evolution with visible light, Angew. Chem. Int. Ed. 51 (2012) 3183–3187.

[16] X. Fan, L. Zhang, M. Wang, W. Huang, Y. Zhou, M. Li, R. Cheng, J. Shi, Constructing carbon-nitride-based copolymers via Schiff base chemistry for visible-light photocatalytic hydrogen evolution, Appl. Catal. B: Environ. 182 (2016) 68–73.

[17] M. Wisniewska, S. Chibowski, T. Urban, Nanozirconia surface modification by anionic polyacrylamide in relation to the solid suspension stability-effect of anionic surfactant addition, Powder Technol. 302 (2016) 357–362.

[18] N. Yuan, L. Xu, H. Wang, Y. Fu, Z. Zhang, L. Liu, C. Wang, J. Zhao, J. Rong, Dual physically cross-linked double network hydrogels with high mechanical strength, fatigue resistance notch-insensitivity, and self-healing properties, ACS Appl. Mater. Interfaces 8 (2016) 34034–34044.

[19] H. Li, X. Wu, S. Yin, K. Katsumata, Y. Wang, Effect of rutile TiO2 on the photocatalytic performance of g-C_3N_4/brookite-$TiO_{2-x}N_y$ photocatalyst for NO decomposition, Appl. Surf. Sci. 392 (2017) 531–539.

[20] H. Li, S. Yin, Y. Wang, T. Sato, Effect of phase structures of $TiO_{2-x}N_y$ on the photocatalytic activity of $CaAl_2O_4$:(Eu,Nd)-coupled $TiO_{2-x}N_y$, J. Catal. 286 (2012) 273–278.

[21] L. Gao, T. Wen, J. Xu, X. Zhai, M. Zhao, G. Hu, P. Chen, Q. Wang, H. Zhang, Iron-doped carbon nitride-type polymers as homogeneous organocatalysts for visible light-driven hydrogen evolution, ACS Appl. Mater. Interfaces 8 (2016) 617–624.

[22] H. Jiang, Q. Wang, S. Zang, J. Li, Q. Wang, Enhanced photoactivity of Sm, N, P-tridoped anatase-TiO_2 nano-photocatalyst for 4-chlorophenol degradation under sunlight irradiation, J. Hazard. Mater. 261 (2013) 44–54.

[23] F. Cheng, H. Wang, X. Dong, The amphoteric properties of g-C_3N_4 nanosheets and fabrication of their relevant heterostructure photocatalysts by an electrostatic re-assembly route, Chem. Commun. 51 (2015) 7176–7179.

[24] G. Zhang, Z. Lan, X. Wang, Conjugated polymers: catalysts for photocatalytic hydrogen evolution, Angew. Chem. Int. Ed. 55 (2016) 2–18.

[25] Y. Zhu, Y. Wang, Q. Ling, Y. Zhu, Enhancement of full-spectrum photocatalytic activity over $BiPO_4$/Bi_2WO_6 composites, Appl. Catal. B: Environ. 200 (2017) 222–229.

[26] Y. Zheng, L. Lin, B. Wang, X. Wang, Graphitic carbon nitride polymers toward sustainable photoredox catalysis, Angew. Chem. Int. Ed. 54 (2015) 12868–12884.

[27] L. Shi, K. Chang, H. Zhang, X. Hai, L. Yang, T. Wang, J. Ye, Drastic enhancement of photocatalytic activities over phosphoric acid protonated porous g-C_3N_4 nanosheets under visible light, Small 12 (2016) 4431–4439.

[28] Y. Fu, T. Huang, B. Jia, J. Zhu, X. Wang, Reduction of nitrophenols to aminophenols under concerted catalysis by Au/g-C_3N_4 contact system, Appl. Catal. B: Environ. 202 (2017) 430–437.

[29] H.J. Li, A.B.W. Sun, L. Sui, D.J. Qian, M. Chen, Preparation of water-dispersible porous g-C_3N_4 with improved photocatalytic activity by chemical oxidation, Phys. Chem. Chem. Phys. 17 (2015) 3309–3315.

[30] Z. Huang, F. Li, B. Chen, G. Yuan, Cycloaddition of CO_2 and epoxide catalyzed by amino- and hydroxyl-rich graphitic carbon nitride, Catal. Sci. Technol. 6 (2016) 2942–2948.

[31] J. Liu, Y. Liu, N. Liu, Y. Han, X. Zhang, H. Huang, Y. Lifshitz, S. Lee, J. Zhong, Z. Kang, Metal-free efficient photocatalyst for stable visible water splitting via a two-electron pathway, Science 347 (2015) 970–974.

[32] Y. Sun, S. Gao, F. Lei, Y. Xie, Atomically-thin two-dimensional sheets for understanding active sites in catalysis, Chem. Soc. Rev. 44 (2015) 623–636.

[33] K. Kang, S. Watanabe, K. Broch, A. Sepe, A. Brown, I. Nasrallah, M. Nikolka, Z. Fei, M. Heeney, D. Matsumoto, K. Marumoto, H. Tanaka, S. Kuroda, H. Sirringhaus, 2D coherent charge transport in highly ordered conducting polymers doped by solid state diffusion, Nat. Mater. 15 (2016) 896–902.

[34] S. Kundu, A. Patra, Nanoscale strategies for light harvesting, Chem. Rev. 117 (2017) 712–757.

[35] X. Fan, L. Zhang, R. Cheng, M. Wang, M. Li, Y. Zhou, J. Shi, Construction of g-C_3N_4-based intramolecular donor-acceptor conjugated copolymers for photocatalytic hydrogen evolution, ACS Catal. 5 (2015) 5008–5015.

[36] D.J. Martin, K. Qiu, S.A. Shevlin, A.D. Handoko, X. Chen, Z. Guo, J. Tang, Highly efficient photocatalytic H_2 evolution from water using visible light and structure-controlled graphitic carbon nitride, Angew. Chem. Int. Ed. 53 (2014) 9240–9245.

[37] W. Xing, G. Chen, C. Li, J. Sun, Z. Han, Y. Zhou, Y. Hu, Q. Meng, Construction of large-scale ultrathin graphitic carbon nitride nanosheets by a hydrogen-bond-assisted strategy for improved photocatalytic hydrogen production and ciprofloxacin degradation activity, ChemCatChem 8 (2016) 2838–2845.

[38] C. Ye, J. Li, Z. Li, X. Li, X. Fan, L. Zhang, B. Chen, C. Tung, L. Wu, Enhanced driving force and charge separation efficiency of protonated g-C_3N_4 for photocatalytic O_2 evolution, ACS Catal. 5 (2015) 6973–6979.

[39] K. Sorathiya, B. Mishra, A. Kalarikkal, K.P. Reddy, C.S. Gopinath, D. Khushalani, Enhancement in rate of photocatalysis upon catalyst recycling, Sci. Rep. 6 (2016) 35075.

[40] X. Mao, C. Fan, Y. Wang, Y. Wang, X. Zhang, RhB-sensitized effect on the enhancement of photocatalytic activity of BiOCl toward bisphenol-A under visible light irradiation, Appl. Surf. Sci. 317 (2014) 517–525.

[41] X. Bai, L. Wang, R. Zong, Y. Zhu, Photocatalytic activity enhanced via g-C_3N_4 nanoplates to nanorods, J. Phys. Chem. C 117 (2013) 9952–9961.